Representation of the Autoconversion from Cloud to Rain Using a Weighted Ensemble Approach: A Case Study Using WRF v4.1.3

Jinfang Yin[1]*, Xudong Liang[1], Hong Wang[2], Haile Xue[1]

1 State Key Laboratory of Severe Weather (LaSW), Chinese Academy of Meteorological Sciences (CAMS), Beijing 100081, China

2 Guangzhou Institute of Tropical and Marine Meteorology, China Meteorological Administration (CMA), Guangzhou 510080, China

Submitted to *Geoscientific Model Development* (GMD)

On 5 July 2021

Corresponding to: Jinfang Yin (yinjf@cma.gov.cn)

Abstract. Cloud and precipitation processes remain among the largest sources of uncertainties in weather and climate modeling, and considerable attention has been paid to improving the representation of the cloud and precipitation processes in numerical models in the last several decades. In this study, we develop a weighted ensemble (named EN) scheme by employing several widely used autoconversion (ATC) schemes to represent the ATC from cloud water to rainwater. One unique feature of the EN approach is that ATC rate is a weighted mean value based on the calculations from several ATC schemes within a microphysics scheme with a negligible increase of computation cost. The EN scheme is compared with the several commonly used ATC schemes by performing real case simulations. In terms of accumulated rainfall and extreme hourly rainfall rate, the EN scheme provides better simulations than that by using the single Berry-Reinhardt scheme which was originally used in the Thompson scheme. It is worth emphasizing, in the present study, we only pay attention to the ATC process from cloud water into rainwater with the purpose to improve the modeling of the extreme rainfall events over southern China. Actually, any (source/sink) term in a cloud microphysics scheme can be treated with the same approach. The ensemble method proposed herein appears to have important implications for developing cloud microphysics schemes in numerical models, especially for the models with variable grid resolution, which would be expected to improve the representation of cloud microphysical processes in the weather and climate models.

1 Introduction

Cloud and precipitation processes and associated feedbacks have been confirmed to cause the largest uncertainties in weather and climate modeling by the Intergovernmental Panel on Climate Change (IPCC) (Houghton et al., 2001). Owing to the complex microphysical processes in clouds and their interactions with dynamical and thermodynamic processes, considerable attention has been devoted to developing cloud microphysics schemes in the numerical weather and climate models in the last several decades, which is summarized in several review articles (e.g., Grabowski et al., 2019; Khain et al., 2015; Morrison et al., 2020). Because of fundamental gaps in the knowledge of cloud microphysics, however, there are still a large number of empirical values derived and assumptions in microphysics schemes based on limited observations, even from numerical simulations (Tapiador et al., 2019). As a result, simulations are quite sensitive to microphysical parameter settings (Falk et al., 2019; Freeman et al., 2019; Gilmore et al., 2004), and thus obvious differences occur frequently from different simulations due to the poor representation of the empirical values and assumptions (Lei et al., 2020; White et al., 2017).

Collision–coalescence between cloud droplets forming raindrops is referred to as the autoconversion (ATC), which is a significant microphysical process in warm clouds. Therefore, the representation of the ATC from cloud water to rainwater is a key aspect of cloud microphysical parameterization. Firstly, raindrop is initiated by the ATC process in warm clouds, which plays a significant role in the onset of a rainfall event. Besides, the ATC process has an important influence on cloud microphysical properties by bridging aerosols, cloud droplets, and raindrops (White et al., 2017). Additionally, local circulation may be modified to a certain extent due to the falling down of the initialized raindrops because of the terminal velocity of the raindrop (Doswell, 2001). Moreover, changes in the rate of ACT had some effect on the lower-tropospheric radiative flux divergence (Grabowski et al., 1999). Consequently, an appropriate representation of the ATC process is helpful for our understanding of cloud micro- and macro-properties, as well as precipitation processes.

Over the last several decades, much attention has been devoted to establishing ATC schemes in atmospheric numerical models, and efforts are under way to create accurate and computationally efficient ATC schemes. Kessler (1969) pioneered a simple scheme in which the ATC rate was connected to cloud water content (CWC), and the scheme has been widely used in bulk microphysics schemes (e.g., Chen and Sun, 2002; Dudhia, 1989; Ghosh and Jonas, 1999; Rutledge and Hobbs, 1984). As an alternate way, Berry (1968) established a more physical formulation in which not only CWC was considered but also cloud droplet number concentration (N_c) and spectral shape parameter of cloud droplet size distribution. The Berry scheme was featured by estimating the time t required for the sixth-moment diameter of the spectral density to reach 80 μm by droplet coalescence, and Simpson and Wiggert (1969) increased the sixth-moment diameter to 100 μm. Ghosh and Jonas (1999) proposed a scheme by combining the advantages of the Kessler and Berry schemes, which allow the use of the simple linear Kessler-type expression and incorporating the effects of different cloud types. On the other hand, several model-derived empirical schemes were established on the basis of sophisticated microphysical simulations (Berry and Reinhardt, 1974; Franklin, 2008; Khairoutdinov and Kogan, 2000; Lee and Baik, 2017). Recently, Some studies (e.g., Franklin, 2008; Li et al., 2019; Onishi et al., 2015; Seifert et al., 2010) the effect of turbulence on ATC have been taken into account. Naeger et al. (2020) proposed that neglect of turbulence influence within an ATC scheme resulted in very weak condensational and collisional growth processes, and thus underpredicted the contribution of warm rain processes to the surface precipitation. More recently, multi-moment schemes were explored, which appeared to improve precipitation simulation to a certain extent (Kogan and Ovchinnikov, 2019).

To date, numerous ATC schemes have been established (Beheng, 1994; Berry, 1968; Berry and Reinhardt, 1974; Caro et al., 2004; Franklin, 2008; Kessler, 1969; Kogan and Ovchinnikov, 2019; Lee and Baik, 2017; Lin et al., 2002; Liu and Daum, 2004; Liu et al., 2006; Manton and Cotton, 1977a; Seifert and Beheng, 2001; Wood et al., 2002; Yin et al., 2015). As noted in previous studies (Gilmore and Straka, 2008; Hsieh et al., 2009; Liu et al., 2006; Xiao et al., 2020; Yin et al., 2015), ATC rates predicted by different schemes can differ by several orders of magnitude for a given CWC. Many previous studies have shown that ATC rates are often overestimated/underestimated by those ATC schemes. For instance, Cotton (1972) pointed out that Kessler's formulation produced the largest error at smaller CWCs, and Berry's formulation consistently resulted in a low rain rate low in the simulated clouds. Iacobellis and Somerville (2006) proposed that the Manton-Cotton parameterization (Manton and Cotton, 1977b) produced much larger values of liquid water path (LWP) than measurements both by satellites and surface-based at the Atmospheric Radiation Measurement (ARM) Program's Southern U.S. Great Plains site. Silverman and Glass (1973) addressed that the Cotton (1972) scheme resulted in a peak cloud water content that occurred earliest at the lowest altitude but has the lowest value as compared with those of the Kessler (1969) and Berry (1968) schemes.

However, Flatøy (1992) stated that Sundqvist's (Sundqvist et al., 1989) and Kessler's (Kessler, 1969) schemes gave comparable results when used a suitable choice of parameters. To the best of our knowledge, however, there is no one ATC parameterization scheme able to provide good results at all times so far, and much effort is necessary for further development of the ATC parameterization (Michibata and Takemura, 2015).

As noted by Morrison et al. (2020), one of the most serious issues of treating microphysics in weather and climate models is the uncertainties in the microphysical process rates owing to fundamental gaps in the knowledge of cloud physics. Posselt et al. (2019) proposed that changes in cloud microphysical parameters produced the same order of magnitude change in model output as did changes to initial conditions, and thus it was important to constraint uncertainties in cloud microphysical processes if possible. Wellmann et al. (2020) also pointed out that model dynamical and microphysical properties were sensitive to both the environmental and microphysical uncertainties, and the latter resulted in larger uncertainties in the output of integrated hydrometeor mass contents and precipitation variables.

There is still a poor representation of the ATC process in weather and climate models, and the potential uncertainties are non-negligible in the ATC schemes (Michibata and Takemura, 2015), and continued advancement of parameterizations require greater knowledge of the underlying physical processes in order to reduce the uncertainties, including from laboratory studies, cloud observations, and detailed process modeling (Randall et al., 2019). Most importantly, representing cloud processes consistently across multi-scales models with an empirical scheme appears to be one of the major challenges in cloud parameterizations

(Randall et al., 2019). To fill this gap, the objective of this paper is to address how to reduce the negative effects of inherent uncertainties in the ATC (from cloud water to rainwater) parameterization within a cloud microphysics scheme to make the weather and climate models behave realistically. To achieve this goal, we design a weighted ensemble (herein abbreviated as EN) scheme to represent the ATC process by employing several widely used ATC schemes within a cloud microphysics scheme.

This paper is organized as follows. An overview of the selected ATC schemes is presented in Section 2. Section 3 describes the approach of the ensemble scheme. The Weather Research and Forecasting (WRF) model configuration and experiment settings are given in Section 4. Simulated results of an extreme rainfall event are presented in Section 5. Finally, conclusions and discussions are given in Section 6.

2 Overview of the selected autoconversion schemes

In the present study, four widely used ATC schemes are selected, including Kessler (1969) (KE) scheme, Berry and Reinhardt (1974) (BR) scheme, Khairoutdinov and Kogan (2000) (KK) scheme, and Liu et al. (2006) (LD) scheme. Depending on the properties of the “bulk” microphysics schemes, the KE scheme is a one-moment scheme, and the BR and KK are double-moment schemes. The LD scheme provides a generalized expression with a smooth transition in the vicinity of the ATC threshold, which is featured by eliminating unnecessary assumptions inherent in the existing Kessler-type parameterizations. It should be noted it is still troublesome to justify in recommending one of the ATC schemes over the other, although those schemes have been extensively tested and widely used in the previous studies (Gilmore and Straka, 2008; Jing et al., 2019; Michibata and Takemura, 2015; White et al., 2017).

2.1 Kessler (KE) scheme

Kessler (1969) pioneered a simple expression in which ATC rate is related to CWC. The KE scheme has been widely used in cloud-related processes in weather and climate numerical models due to its simplicity. The ATC rate from cloud water to rainwater is expressed as

$$P_{ATC-KE}[\mathrm{kg\,kg^{-1}\,s^{-1}}] = r_a a(q_c - q_0)H(q_c - q_0) \quad \begin{cases} q_c - q_0 \geq 0,\ H(q_c - q_0) = 1, \\ q_c - q_0 < 0,\ H(q_c - q_0) = 0. \end{cases}, \qquad (1)$$

where a =0.001 s^{-1} is a time constant, H is the Heaviside function, q_c is CWC in the unit of kg m^{-3}, and r_a is air density. The threshold q_0 is the minimum CWC below which there is no ATC from cloud water to rainwater (Fig. 1a). Owing to the simple and linear expression, the KE scheme is computationally straightforward to implement in numerical models. However, the major limitation of the KE scheme results in its inability to identify different conditions such as maritime and continental clouds (Ghosh and Jonas, 1999). More specifically, the KE scheme only took CWC into account, while cloud number concentration was not incorporated. This may partially explain the KE scheme yielded the large errors at low CWC proposed by Cotton (1972). Besides, it is impossible to obtain the thresholds directly used in the scheme from observations at present, while cloud microphysical processes are sensitive to the thresholds (Plsselt et al., 2019). A modified Kessler scheme was proposed by Yin et al. (2015) in which q_0 is diagnosed as a function of altitude by using a CWC-height relationship which was derived from CloudSat observations. In order to get reasonable results, different values of q_0 were chosen by various studies. For instance, a value of 0.5 g m^{-3} is given in Kessler's (1969), Reisner (1998), and Schultz (1995). Thompson (2004) reduced to a small value of

0.35 g m^{-3}. Kong and Yau (1997) and Tao and Simpson (1993) gave a value of 2 g kg^{-1}, while a small value of 0.7 g kg^{-1} was assigned in Chen and Sun (2002). In this work, the same value of 0.5 g m^{-3} as that assigned in Kessler's (1969) is chosen.

2.2 Berry-Reinhardt (BR) scheme

Berry and Reinhardt (1974) proposed a physical formulation to represent the ATC process in clouds, which is given by

$$P_{ATC-BR}[\mathrm{kg\,kg^{-1}\,s^{-1}}]=\frac{2.7\times10^{-2}\,r_w q_c\left[\frac{1}{16}\times10^{20}D_{mean}^{4}(1+m)^{-0.5}-0.4\right]}{\frac{3.7}{r_a q_c}\left[0.5\times10^{6}D_{mean}(1+m)^{-1/6}-7.5\right]^{-1}}. \qquad (2)$$

Here, m represents shape parameter of a gamma distribution, r_w is liquid water density. D_{mean} is the mean diameter (unit in m) of the total cloud droplets, which is computed from

$$D_{mean}=\left(\frac{6q_c}{p r_w N_c}\right)^{1/3}. \qquad (3)$$

Here, p is the circumference ratio. The BR scheme was developed theoretically in which not only CWC but also cloud number concentration was incorporated. An important characteristic is that maritime and continental clouds can be differentiated by the BR scheme using different parameters (Simpson and Wiggert, 1969; Pawlowska and Brenguier, 1996). Cotton (1972) argued that the BR scheme seems to underestimate rain formation in their simulations. Compared to KE, the BR scheme has treated the process more rigorously (Ghosh and Jonas, 1999). It should be noted that ATC rates given by BR are quite sensitive to N_c (Fig. 1b).

2.3 Khairoutdinov-Kogan (KK) scheme

Khairoutdinov and Kogan (2000) proposed a computationally efficient and relatively simple scheme, which aims at large-eddy simulation (LES). One of the advantages is that there is no need to define a threshold, and this scheme has been broadly used in numerical models (e.g., Morrison et al., 2009). The ATC rate is given by

$$P_{ATC\text{-}KK}[\mathrm{kg\,kg^{-1}\,s^{-1}}]=1350q_c^{2.47}(N_c\times10^{-6})^{-1.79}. \qquad (4)$$

The KK scheme uses a simple power-law expression based on a series of large-eddy simulations. Generally speaking, the autoconversion rate increases with increasing CWC and/or decreasing cloud number concentration. The simple expression is a key advantage of the KK scheme, which makes it possible to analytically integrate the microphysical process rates over a probability density function (Griffin and Larson, 2013). In view of Fig. 1c, the KK scheme has a strong dependency on N_c. Increasing N_c from 100 to 500, ATC rates decrease dramatically, especially at the CWCs over 1.0 g m^{-3}. Unlike other schemes, ATC is allowable in the KK scheme even with very low CWCs, which might lead to overestimations under such conditions.

2.4 Liu-Daum-McGraw-Wood (LD) scheme

A generalized ATC parameterization was proposed by Liu et al. (2006). The approach improved the representation of the threshold function by applying the expression for the critical radius derived from the kinetic potential theory. The parameterization is given by

$$P_{ATC-LD}[\mathrm{kg\,kg^{-1}\,s^{-1}}]=kb^6q_c^3N_c^{-1}\left\{1-exp[-(1.03\times10^{16}N_c^{-3/2}q_c^2)^m]\right\}. \qquad (5)$$

Here, κ(=1.1×10^{10} kg^{-2} m^3 s^{-1}) is a constant. β is a parameter related to the relative dispersion e of cloud droplets, which is obtained from

$$b=\left[\frac{(1+3e^2)(1+4e^2)(1+5e^2)}{(1+e^2)(1+2e^2)}\right]^{\frac{1}{6}}. \qquad (6)$$

Here, a value of 0.5 is assigned to e following Liu et al. (2006). The LD scheme assumes that autoconversion rate is determined by CWC, cloud number concentration, and relative dispersion of cloud droplets. Xie and Liu (2015) suggested that the LD scheme considering spectral dispersion was more reliable for improving the understanding of the aerosol indirect effects, compared to the KE and BR schemes. Note that the LD scheme is characterized by the smooth transition in the vicinity of the ATC threshold.

3 Description of the ensemble (EN) scheme

As has been mentioned above, ATC rates predicted by different schemes can differ by several orders of magnitude for a given CWC. Nowadays, it is still troublesome to judge which scheme is preferred to others at all times (Ghosh and Jonas, 1999; Jing et al., 2019; Liu et al., 2006; Michibata and Takemura, 2015). To the best of our knowledge, each one has its advantages and disadvantages. Keeping this fact in our mind, we propose a weighted (the EN) scheme by employing the above-listed four commonly used ATC schemes, and the weighted ensemble ATC rate ($P_{ATC\text{-}EN}$) is given by

$$P_{ATC-EN}[\mathrm{kg\,kg^{-1}\,s^{-1}}]=\frac{w_{KE}P_{ATC-KE}+w_{KK}P_{ATC-KK}+w_{LD}P_{ATC-LD}+w_{BR}P_{ATC-BR}}{w_{KE}+w_{KK}+w_{LD}+w_{BR}}\,. \quad (7)$$

Here, w_{xx}, referring to that for KE, KK, LD, and BR, respectively, is the weight of each ATC scheme. It is worth noting that Eq. (7) is easily reduced into any single scheme form by setting all w_{xx} values of 0 except for one of them. Therefore, it is a flexible way to use any one or more schemes to calculate $P_{ATC\text{-}EN}$ by adjusting w_{xx}. Of course, it is also convenient to reduce the effect of any one of them by giving a small value of w_{xx}. At present, the same weights with the value of 1.0 are assigned for all schemes for simplicity. Note that, the weights can be modulated according to weather conditions. One of the features of the EN scheme is that the weighted mean is calculated within a microphysics scheme, and the increase of computation cost is negligible.

Similar to an ensemble prediction system (Lewis, 2005), the EN scheme is expected to reduce the potential uncertainties from the use of any ATC scheme alone under various CWC conditions. For example, no cloud water converts into rain water in the KS scheme when the cloud water is less than the threshold, while in the KK scheme it always occurs. However, the KS scheme has much higher ATC rates owing to the linear relationship (Eq. 1), compared to those of the KK scheme. Most importantly, the EN scheme is beneficial for the multi-scale numerical weather and climate modeling systems, especially for variable resolution models (e.g., the Model for Prediction Across Scales, MPAS (Skamarock et al., 2012), the Global-to-Regional Integrated forecast SysTem, GRIST, (Zhang et al., 2019)), because it is flexible to represent cloud processes consistently across all model scales under the various conditions. Depending on grid distance, one or more schemes can be used independently in a variable resolution model. For example, we assign all w_{xx} to 0 except for w_{KK} in the fine grid distance region, and a mean value from the calculation of two or more schemes is utilized in the grid distance transition zone.

To facilitate comparisons among the aforementioned ATC schemes, an idealized experiment is performed with a wide range of CWCs in the calculations. A rough value of N_c is set to 300 cm^{-3} in the continental clouds (e.g., Hong and Lim, 2006; Thompson et al., 2008). For convenience, air density is approximately fixed at 1.29×10^{-3} g cm^{-3} here. It is noteworthy that the value of 2 is assigned to μ for both BR and LD schemes. Figure 2 compares the EN scheme with the selected four schemes with a wide range of CWCs from 0.01 to 1.0 g m^{-3}. One can see that all the schemes yield ATC rates of ~10^{-9} g cm^{-3} s^{-1}, although there are significant discrepancies among the different schemes. For the KS scheme, the ATC of cloud water to rain water does not start until the CWC exceeds the threshold q_0 (Eg. 1). In contrast, the other schemes are allowable even given fair low CWCs.

Comparatively speaking, both KS and LD predicts a larger ATC rate than the other ATC schemes (the BR or KK scheme) for a given CWC. As for the former group, LD yields the largest ATC rate with CWC below 0.6 g m^{-3}, while KS generates the largest ATC with CWC over 0.6 g m^{-3}. Wood and Blossey (2005) argued that the ATC rate defined in LD would give the total rate of mass coalescence among cloud droplets and is typically much larger than the true ATC rate. With N_c fixed at 300 cm^{-3}, the BR scheme shows close ATC rates to those of KK. Note that the KK scheme, originally developed for the Large Eddy Simulation (LES) model, yields the lowest ATC rate, followed by the BR scheme. The EN scheme provides a similar pattern to LD, but nearly half ATC rates of those are yielded by the latter. It should be emphasized that ATC rates are fairly sensitive to N_c (Fig. 1), and a higher or lower N_c would cause great changes.

4 Simulations of an extreme rainfall event

4.1 Overview of the rainfall event

An extreme rainfall event hit Guangzhou megacity in the early morning hours of 7 May 2017. Within 18 hours (during the period of 2000 Beijing standard time (BST, BST = UTC + 8) 6 May to 1400 BST 7 May), there were 12 rain gauge stations over 250 mm during the rainfall process. The spatial distribution of the rainfall appears two heavy rainfall cores over

Jiulong (JL) and Huashan (HS) regions (Fig. 3a). The event was featured by the heaviest rainfall in Guangzhou megacity over the past six decades with the maximum total amount of 542 mm within 18 hours at JL station (Fig. 3a). It also broke the record of 3-h accumulated rainfall amount with the value of 382 mm. Another marked feature of this rainfall event was its extreme hourly rainfall rate of 184 mm h^{-1}, which is the second-highest over the Guangdong Province, China.

4.2 Model configuration and experiment settings

This event was well simulated and investigated by Yin et al. (2020), focusing on the effects of urbanization and orography. The WRF model configurations, and initial and boundary conditions are the same as Yin et al. (2020) except for updating to the WRF-ARW(v4.1.3) model (Skamarock et al., 2019) with several minor bugs fixed. For convenience, an overview of the WRF model configures is presented here. The triple nested domains have x, y dimensions of 313×202, 571×334, and 862×541 with grid sizes of 12, 4, and 1.33 km, respectively. The WRF model physics schemes are configured with the Thompson microphysics scheme (Thompson et al., 2008) with the modifications of ATC parameterization, the rapid radiative transfer model (rrtm) (Mlawer et al., 1997) for both shortwave and longwave radiative flux calculations, the Yonsei University (YSU) planetary boundary layer (PBL) scheme (Hong et al., 2006), the MM5 Monin-Obukhov scheme for the surface layer (Janjić, 1994), and the Noah-MP land-surface scheme (Niu et al., 2011). The Kain cumulus parameterization scheme (Kain, 2004) is utilized for the outer two coarse resolution domains, but being bypassed in the finest domain. All the three nested domains of the WRF model are integrated for 18 hours, starting from 2000 BST 06 May 2017, with outputs at 6-min intervals. The initial and outermost boundary conditions are interpolated from the National Centers for Environmental Prediction (NCEP) Global Forecast System 0.25 degree re-analysis data at 6-h intervals. In order to introduce realistically the UHI effects of the Guangzhou metropolitan region, the Four-Dimension Data Assimilation (FDDA) functions are activated (Reen, 2016) by performing both the surface observation nudging and the analysis nudging from 2000 BST 6 to 0800 BST 7 May 2017. Please refer to Yin et al. (2020) for more details about the model configuration.

As has been addressed above, it is convenient to conduct a simulation with any of the above-listed ATC schemes alone. In total, two experiments were carried out with the EN and BR schemes. It should be noted that the BR scheme was used originally in the Thompson scheme, and the EN was newly coupled into the Thompson scheme in this work.

5. Results

5.1 Spatial distribution of accumulated rainfall

Figure 3 compares the spatial distribution of 18-h simulated total rainfall from the simulations with the EN and BR schemes to the observed. Generally speaking, both schemes are able to capture the main characteristics of the extreme rainfall event. One can see that the simulated rainfall amount compares favorably to the observed both at HS and JL, although the JL storm has a 10-15 km eastward location shift. Yin et al. (2020) argued that the location errors may be related to large-scale meteorological conditions. Comparatively speaking, the EN and BR schemes performed better than others. The two centralized rainfall cores over HS and JL were successfully captured by the EN and BR schemes, with the simulated heaviest rainfall amount of 537 mm and 569 mm, respectively (Fig. 3b,c). As for the EN scheme (Fig. 3b), the simulated 18-h total rainfalls were 320 mm and 537 mm over HS and JL, respectively, which was close to the observations of 341 mm and 542 mm (Fig. 3a). Similarly, the BR scheme performed equivalently to the EN scheme, with the maximum rainfall of 347 mm and 569 mm over Huashan and Jiulong regions, respectively (Fig. 3c). Note that the simulated heaviest over the Huashan region were comparative among each other. In view of the results, we will compare the maximum hourly rainfall rates near JL from the simulations of the EN and BR schemes to that of observations in the next sections. It should be noted the results in the present study are a little better than (or equivalent to at least) those in Yin et al. (2020) because of the update of the WRF version4.1.3 model with some improvements in dynamical framework and bug fixes.

5.2 Evolution of the simulated hourly rainfall

Figure 4 shows the observed and simulated time series of hourly maximum rainfall rates over the Jiulong region. The observed peak rainfall near JL occurred at 0600 BST 7 May with the hourly rates of 184 mm hr^{-1}. However, the simulated peak rainfall from the EN scheme took place at 0700 BST 7 May, which was about 1 h later than the observed, with the hourly rates of 151 mm hr^{-1}. As for the BR scheme, the simulated peak rainfall rate occurred two hours later, with the value of 144 mm hr^{-1}. As a matter of fact, both EN and BR schemes under-predicted the peak hourly rainfall rate near JL. It is worthy to note that the observed timings of initiating and ending of the extreme rainfall production episode, i.e., near 0300 and 1000 BST 7 May, respectively, were reproduced successfully. However, both simulated peak rates occurred later than the observed due to the slower increases in rain-producing rates than the observed. More specifically, the observed hourly rate increased from about 16 mm hr^{-1} to 184 mm hr^{-1} just in one hour (i.e., from 0500 to 0600 BST). However, the simulated from the EN scheme increased from 0.3 mm hr^{-1} at 0400 BST to about 79 mm hr^{-1} at 0600 BST, and then to 151 mm hr^{-1} at 0700 BST 7 May. As for the simulated with the BR scheme, it increased from 2 mm hr^{-1} at 0400 BST to about 104 mm hr^{-1} at 0700 BST, and then to 144 mm hr^{-1} at 0800 BST 7 May. One unique feature of the observations was the rapid increase of the hourly rainfall rate. The rainfall produced by the EN scheme peaked within 2 h while the BR scheme peaked over a period of 4 h. Additionally, both the simulated rainfall rates decrease for several hours. Generally speaking, the EN scheme performed much closer to the observed, compared to that of the BR scheme. Note that the longer heavy rainfall period from the BR scheme contributed partially to the over-prediction of the 18-h accumulated rainfall (Fig. 3c).

5.3 Evolutions of radar reflectivity

In view of the performance of the accumulated rainfall and the maximum hourly rainfall rates, we only compare the radar reflectivity from the simulations with the EN scheme to the results of the BR scheme. Figure 5 exhibits the structures and evolutions of convective cells over JL region by comparing the simulated composite radar reflectivity to the observed. The first well-organized radar echo formed near 0000 BST over the Huashan region (not shown), which was located at the northern edge of a surface high-θ_e (equivalent potential temperature) tongue with significant convergence. As the southeasterly flow moved slowly eastward and the cold outflows resulted from previous convection, the Huashan storm dissipated while the storm began to develop over the Jiulong region, both in its size and in intensity (Fig. 5a). The storm rapidly intensified during the period from 0430 to 0530 BST, with the peak reflectivity beyond

55 dBZ near the leading edge (Fig. 5a,b). The Jiulong storm moved fairly slowly, keeping more or less quasi-stationary shortly after its formation (Fig. 5a-c). Both the quasi-stationary nature and intense radar reflectivity explain the extreme rainfall production rate occurring at JL during the 1-h period of 0500 - 0600 BST. Subsequently, the Jiulong storm weakened, but its associated peak radar reflectivity still remained over 50 dBZ, which was consistent with the continued generation of significant rainfall near JL until 0800 BST (Fig. 4).

It is obvious that both the EN and BR schemes captured the development of the Jiulong storm, with the main features that were similar to the observed, including quasi-stationary nature, southeastward expansion, and concentrated strong radar reflectivity during the extreme rainfall stage. Both simulations successfully generated a lower-θ_e pool with a distinct outflow boundary interacting with the moist southeasterly flow near the ground. It should be noted that the initiation and organization of both simulated Jiulong storms were about 1.7 h later than the observed, and it occurred at a location nearly 10-15 km kilometers to the east of the observed one. Generally speaking, both simulations with the EN and BR schemes produced extreme rainfall amounts close to those observed and their spatial distributions agree well with observations.

In terms of the spatial distribution of radar reflectivity, similar patterns can be seen between the EN and BR schemes in the early stage before 0712 UTC, while differences are visible at the extreme rainfall stage (Fig. 5e,h). One can find that the Jiulong storm simulated with the EN scheme (Fig. 5f) developed more rapidly than that from the BR scheme, almost 1 h earlier than the latter (Fig. 5i). This was consistent with the timing lag in the hourly extreme rainfall production (Fig. 4). Clearly, the ACT process has an important influence on the convective development of deep convection associated with the extreme rainfall produced within the Jiulong storm, which will be explored in view of the cloud microphysical processes in the next section.

5.4 The Effects on Macro- and Micro-physical Processes

The spatial distribution of hourly rainfall, and temporal-averaged surface temperature and horizontal wind during the period from 0600 BST to 0700 BST from the simulations with the EN and BR schemes are displayed in Fig. 6. As has been stated above, the total rainfall shows a slight difference between EN and BR over the Jiulong region (Fig. 3b,c). In view of the spatial distribution of the hourly rainfall during the period (i.e., 0600 BST to 0700 BST 7) when maximum hourly rainfall occurred (Fig. 6), the EN scheme generated a larger rainfall area and a stronger rainfall rate than those of the BR scheme, although both schemes produced similar spatial distribution patterns in rainfall area, and temporal-averaged surface temperature and horizontal wind filed. The result was consistent with the idealized experiments given in Fig. 2. For a given CWC, the EN scheme had a larger ATC rate, compared to the BR scheme, and the difference becomes obvious with the increase of CWC. Consequently, the EN scheme produced more rain water of small- to middle size, compared to the BR scheme. The larger rain water was favorable for the coalescence of large precipitation particles from the upper levels, which made the larger contribution to the extreme rainfall rate. This is why the EN scheme produced larger rainfall than the BR scheme. The result was consistent with Fu and Lin (2019) in which temporal and spatial extent of the “vigorous rain formation region” where most of the rain was produced. Those features can also be viewed from the vertical sections in Fig. 7. One can see that the largest radar reflectivity reaches the ground, like a bell on the ground (Fig. 7a). This unique feature was reported by Li et al. (2020) based on the observations from the S-band dual-polarization radar at Guangzhou station, Guangdong Province, China. The bell-shaped radar reflectivity was consistent with the episode of the extreme hourly rainfall. The strong radar reflectivity mainly resulted from raindrops coalescence owing to the higher number concentration raindrop in the lower levels (Bao et al., 2020). That is to say, collecting rain water by the collision-coalescence process at the lower levels helped create a large rainfall rate at the ground. As for the BR scheme (Fig. 7b), a middle-level radar reflectivity core was obvious above nearly 1 km up to 4 km, indicating that raindrops coalescence occurred intensively between those levels and evaporation of raindrops was significant below 1 km. The evaporation near above the surface was a considerable factor abating the surface rainfall rate. In view of the vertical distribution of radar reflectivity, the EN scheme generated a maritime-like convective storm, whereas the convective storm simulated by the BR scheme was close to continental-like convection. It should be noted that except for evaporation, large particle (raindrop) breakup can lead reflectivity values to decrease toward the surface because reflectivity is much sensitive to raindrop size. In the present case, the evaporation of raindrops was remarkable. However, a slight difference was found in differential reflectivity Zdr in the lower levels, indicating that large particle (raindrop) breakup was weak.

Both the EN and BR schemes provide tilted storms in view of vertical cross from south to north through the extreme rainfall. During this episode, the updraft was dominant in the storm, and a weak downdraft occurred in the lower levels at the back of the convective storm. Besides, both EN and BR reproduced very close thermal patterns in terms of potential temperature. Note that the EN scheme had a slightly weaker updraft than that of the BR scheme, although only make the modifications in the ATC parameterization in the microphysics scheme (Fig. 7a,b), suggesting that change in cloud microphysical processes can lead to some variations in dynamical processes.

The differences between the EN scheme and BR schemes in updraft can be also viewed from the cumulative contoured frequency by altitude diagrams (CCFAD) given in Fig. 8. CCFAD presents the percentage of horizontal grid points with vertical motion weaker than the abscissa scaled value for a given height (Yuter and Houze, 1995). In this study, vertical speeds are binned with intervals of 1 m s^{-1} based on the eleven model outputs with six-minute intervals during the severe rainfall episode from 0600 BST to 0700 BST 7 May 2017. Generally speaking, the EN scheme shows similar CCFAD patterns to those of the BR scheme. However, there are still differences in the vertical motion. One can see there was a slight weaker core but lower in the EN scheme simulation, compared to those of the BR scheme. During the severe rainfall episode, the EN scheme produced the largest updraft nearly 15 m s^{-1} at 5 km level, while that was about 16 m s^{-1} at 6 km level given by the BR scheme. In contrast, updrafts below 6 m s^{-1} occurred more frequently in EN than that in the BR scheme. Overall, the EN scheme provided a larger updraft area but weaker in upward speed, compared to those in BR scheme. This is why the EN scheme had a larger spatial distribution of rainfall than that of the BR scheme (Fig. 6a,b). Note that both EN and BR schemes had a slight difference in downdrafts in vertical distribution and the downdraft was mainly located below 2 km, which were also visible in the vertical cross sections (Fig. 7a,b).

As has been noted above, both the EN and BR schemes produced very close dynamical patterns except for updrafts. However, differences were remarkable in cloud microphysical processes. Figure 9 compares the temporal evolution of hydrometeors between the EN and BR schemes. One can see that the EN scheme (Fig. 9a-f) produced similar hydrometeors patterns to those of the BR scheme (Fig.9g-i). Overall, graupel was dominant above the melting layer, while rainwater was considerable below the melting layer. Previous studies (Franklin et al., 2005; Krueger et al., 1995; McCumber et al., 1991; Yin et al., 2018) proposed that graupel was dominant in the tropical and subtropical clouds owing to plentiful water vapor. Overall, the EN scheme mainly increased rainwater content and graupel, while only slight differences in cloud water, cloud ice, snow, and water vapor, compared with those of the BR scheme (Fig. 9m-r).

In terms of the difference in rainwater and graupel between the EN and the BR schemes (Fig. 9m-r), we find that the ATC rate of the EN scheme played an important role in the development of deep convection. Compared to the BR scheme, the higher ATC rate of the EN scheme quickly produced more considerable number of small precipitation-sized drops within updrafts in moderate- and lower-levels, and more of the small size raindrops were lofted by the updrafts above the 0°C level and subsequently were fed for ice processes. Within this graupel coexisted with more small supercooled rainwater region, stronger riming occurred between ice particles and the small size raindrops. Consequently, more of the small supercooled raindrops were converted into graupel by ice cloud microphysical processes such as riming, leading to a more rapid graupel production. At the same time (Fig. 9q), more supercooled raindrops froze becoming more graupel embryos since bigger raindrops freeze at warmer temperatures than smaller cloud droplets, and continue to grow by riming and/or other processes. Consequently, graupel was increased at high altitude (above the 0°C) levels. It is well known that bigger water drops freeze at warmer temperatures than small drops. Therefore, partial the small raindrops froze into graupel and snow particles, which contributes to the increment in graupel and snow. Generally, a graupel particle has a larger size than a raindrop with a given mass. Therefore, the larger graupel particle can collect more particles as they fall down in the storm, which helped create the surface heavy rainfall rate. One can see that the graupel increased rapidly nearly 12 minutes after the appearance of increasing supercooled rain (Fig. 9n). It should be noted we try to understand cloud microphysical processes in the extreme rainfall based on our knowledge at present, and thus a rigorous validation is required by comparing hydrometeors sink and terms in a future study.

As the increased graupel passed by the melting level, they started to melt leading to more raindrops. In view of the strong radar reflectivity near the surface in Fig. 7a, the raindrops from upper levels grew rapidly by collecting raindrops in the lower levels. In this way, the extreme rainfall rate was generated in such a more rapid and efficient approach, compared to those of the BR scheme. During this stage, the increased ATC rate was linked to ice-phase processes and modified graupel fraction in the upper levels above the 0°C. As has been mentioned earlier, the increased ATC rate played a certain role in dynamic feedbacks, and the degree of modulation of water vapor, cloud water, cloud ice, and snow by the increased ATC rate was negligible. These findings indicate that increased ATC rate was important in the extreme rainfall that involved ice-phase processes of graupel above the 0°C levels and warm-rain processes of raindrops in the lower levels. To summarize, the higher

ATC rate of the EN scheme produced more small precipitation-sized drops, and some of the small size raindrops were lofted to the upper levels above the 0°C. Consequently, more graupel was generated by riming and freezing processes. The rapid production of graupel played a significant role in the development of extreme rainfall. Collision and coalescence processes between liquid particles appeared to be the mechanism of radar reflectivity increment toward the surface within the storm core region.

We proposed the influence mechanism of the ATC rate on the extreme rainfall by comparing the simulated results between the EN scheme and the BR scheme. However, there are still some limitations in figuring out the complete effects of the increasing ATC rate on microphysical and dynamical processes at present because those processes are entangled with complicated interactions. Therefore, a better choice is to separate the effects on each process by conducting high-resolution simulations with a sophisticated model, such as the approach of Grabowski (2014). Certainly, the best way is to perform offline testing based on in-situ observations, as was done by Wood (2005). Keeping those issues in our mind, further work is needed to address this question.

6 Conclusions and Discussion

In this study, we designed an ensemble (EN) approach to improving ATC process description in the cloud microphysics schemes. One unique feature of the EN approach is that the ATC rate is a mean value based on the calculations from several widely used ATC schemes. Similar to ensemble prediction, this approach is aimed to improve the representation of the ATC rate in case it has been treated by using an ATC scheme alone in the cloud microphysics schemes. At present, the four widely used ATC schemes are selected, including Kessler (1969) scheme, Berry and Reinhardt (1974) scheme, Khairoutdinov and Kogan (2000) scheme, and Liu et al. (2006) scheme. In the EN scheme, each scheme is assigned a weight (Eq. 7) in order to modulate its importance. Certainly, the EN scheme is easily reduced into any single scheme by setting all w_{xx} values of 0 except for one of them. It is also convenient to reduce the effect of a scheme by giving a small value of w_{xx}, even removing the effect of a scheme by assigning a value of weight to 0. Under this framework, the ATC rates from the EN scheme are compared to those from each of the several commonly used schemes by ideal experiments, and a series of simulations are carried out for an urban-induced extreme rainfall event over Southern China by using the EN, KE, BR, KK, and LD schemes which have been coupled into the Thompson scheme in the WRF model (Thompson et al., 2008) in this work. The results show that the EN scheme provides better simulations, compared to those from any single ATC scheme used alone.

In this study, the ensemble approach has been employed to represent the ATC process in the Thompson cloud microphysics scheme, which shows some advantages for simulation of the extreme rainfall event, occurred on 7 May 2017 over southern China. It is important to acknowledge that the conclusions are drawn from just one case study, and have not been validated under a wider range of conditions over the world. In the forthcoming studies, a systematic assessment of heavier rainfall events is planned to better understand the performance of the EN scheme. It should be noted that there are still some limitations to the EN scheme in the present study. Although a large number of ATC schemes are available, most among them are not employed as ensemble members. For example, the Franklin scheme

(Franklin, 2008) took the effect of turbulence on the ATC process into account, which plays important role in precipitation development (Chandrakar et al., 2018; Seifert et al., 2010). Furthermore, equal weights were used in the present study for convenience. In other words, the selected schemes have the same effect on the ATC rate. Moreover, only conventional verifications were carried out, and the dependency of the performance of the ATC schemes on the model resolution was not considered in this study. A further examination with new approaches (e.g., Wood, 2005; Grabowski, 2014) might provide important insights in the near future.

ATC is an important process of raindrop initiation in the low-level clouds in general circulation models (GCMS), which has remarkable effects on the models' results (e.g., Golaz et al., 2011; Roy et al., 2021). The ATC is sensitive to an ATC scheme, even a parameter, due to heterogeneous cloud properties over the world. Consequently, the EN scheme may be a good option for GCMS in which there are various possible cloud conditions. It is worth emphasizing that we focus our attention on the ATC from cloud water into rainwater at present. Certainly, any source/sink term in a cloud microphysics scheme can be dealt with with the same method. Since developing a "unified" cloud scheme appears to be a significant part of weather and climate model development in the coming years (Randall et al., 2019), the EN approach may be a practicable way to reduce the potential uncertainty in cloud and precipitation physical process, which will contribute to more accurate numerical model development.

Code and data availability: The source code of the Weather Research and Forecasting model (WRF v4.1.3) is available at https://github.com/wrf-model/WRF/releases (last access: July

2021). Modified WRF model codes and initial and boundary data used for the simulations are available on Zenodo (https://doi.org/10.5281/zenodo.5052639). The National Centers for Environmental Prediction (NCEP) Global Forecast System 0.25 degree final-analysis data at 6-h intervals used for the initial and boundary conditions for the specific analysed period can be downloaded at https://rda.ucar.edu/datasets/ds083.2/.

Competing interests: The author declares no competing interests.

Author contributions. J. Yin developed the weighted ensemble scheme and coupled the scheme into the WRF model, with contributions from X. Liang. J. Yin tested and verified the scheme with contributions from X. Liang, H. Wang, and H Xue. J. Yin wrote the manuscript, and all the authors continuously discussed the results and contributed to the improvement of the paper text.

Acknowledgements: This study is jointly supported by the National Key Research and Development Program of China (2018YFC1507404 and 2017YFC1501806), and National Natural Science Foundation of China (42075083). The authors also acknowledge the use of the NCAR Command Language (NCL) in the analysis of some of the WRF Model output and the preparation of figures. The authors are thankful to the Chief editor (Astrid Kerkweg), the handling topical deitor (David Topping), and two anonymous reviewers for their help improving the manuscript.

References:

Bao, X., Wu, L., Tang, B., Ma, L., Wu, D., Tang, J., Chen, H., and Wu, L.: Variable Raindrop Size Distributions in Different Rainbands Associated With Typhoon Fitow (2013), J. Geophys. Res.: Atmos., 124, 12262-12281, https://doi.org/10.1029/2019JD030268, 2019.

Bao, X., Wu, L., Zhang, S., Li, Q., Lin, L., Zhao, B., Wu, D., Xia, W., and Xu, B.: Distinct Raindrop Size Distributions of Convective Inner- and Outer-Rainband Rain in Typhoon Maria (2018), J. Geophys. Res.: Atmos., 125, e2020JD032482, https://doi.org/10.1029/2020JD032482, 2020.

Beheng, K. D.: A parameterization of warm cloud microphysical conversion processes, Atmos. Res., 33, 193-206, https://doi.org/10.1016/0169-8095(94)90020-5 , 1994.

Berry, E. X.: Modification o the warm rain process. Preprints, First National Conf. on Weather Modification, Albany, NY, Amer. Meteor. Soc., 81–88, 1968.

Berry, E. X. and Reinhardt, R. L.: An Analysis of Cloud Drop Growth by Collection Part II. Single Initial Distributions, J. Atmos. Sci., 31, 1825-1831, https://doi.org/10.1175/1520-0469(1974)031<1825:aaocdg>2.0.co;2, 1974.

Caro, D., Wobrock, W., Flossmann, A. I., and Chaumerliac, N.: A two-moment parameterization of aerosol nucleation and impaction scavenging for a warm cloud microphysics: description and results from a two-dimensional simulation, Atmos. Res., 70, 171-208, http://dx.doi.org/10.1016/j.atmosres.2004.01.002, 2004.

Chandrakar, K. K., Cantrell, W., and Shaw, R. A.: Influence of Turbulent Fluctuations on Cloud Droplet Size Dispersion and Aerosol Indirect Effects, J. Atmos. Sci., 75, 3191-3209, https://doi.org/10.1175/JAS-D-18-0006.1, 2018.

Chen, S.-H. and Sun, W.-Y.: A One-dimensional Time Dependent Cloud Model, J. Meteor. Soc. Japan, 80, 99-118, https://doi.org/10.2151/jmsj.80.99, 2002.

Cotton, W. R.: Numerical Simulation of Precipitation Development in Supercooled Cumuli—Part I, Mon. Wea. Rev., 100, 757-763, https://doi.org/10.1175/1520-0493(1972)100<0757:NSOPDI>2.3.CO;2, 1972.

Doswell, C. A., III: Severe Convective Storms—An Overview, Meteor. Monogr., 50, 1-26, https://doi.org/10.1175/0065-9401-28.50.1, 2001.

Dudhia, J.: Numerical Study of Convection Observed during the Winter Monsoon Experiment Using a Mesoscale Two-Dimensional Model, J. Atmos. Sci., 46, 3077-3107, https://doi.org/10.1175/1520-0469(1989)046<3077:NSOCOD>2.0.CO;2, 1989.

Falk, N. M., Igel, A. L., and Igel, M. R.: The relative impact of ice fall speeds and microphysics parameterization complexity on supercell evolution, Mon. Wea. Rev., 147, 2403-2415, https://doi.org/10.1175/MWR-D-18-0417.1, 2019.

FlatøY, F.: Comparison of two parameterization schemes for cloud and precipitation processes, Tellus A: Dyn. Meteoro. Ocean., 44, 41-53, https://doi.org/10.3402/tellusa.v44i1.14942, 1992.

Franklin, C. N.: A Warm Rain Microphysics Parameterization that Includes the Effect of Turbulence, J. Atmos. Sci., 65, 1795-1816, https://doi.org/10.1175/2007JAS2556.1, 2008.

Franklin, C. N., Holland, G. J., and May, P. T.: Sensitivity of Tropical Cyclone Rainbands to Ice-Phase Microphysics, Mon. Wea. Rev., 133, 2473-2493, https://doi.org/10.1175/MWR2989.1, 2005.

Freeman, S. W., Igel, A. L., and van den Heever, S. C.: Relative sensitivities of simulated rainfall to fixed shape parameters and collection efficiencies, Quart. J. Royal Meteor. Soc., 145, 2181-2201, https://doi.org/10.1002/qj.3550, 2019.

Fu, H. and Lin, Y.: A Kinematic Model for Understanding Rain Formation Efficiency of a Convective Cell, J. Adv. Model. Earth Sy., 11, 4395-4422, https://doi.org/10.1029/2019MS001707, 2019.

Ghosh, S. and Jonas, P. R.: On the application of the classic Kessler and Berry schemes in Large Eddy Simulation models with a particular emphasis on cloud autoconversion, the onset time of precipitation and droplet evaporation, Ann. Geophys., 16, 628-637, https://doi.org/10.1007/s00585-998-0628-2, 1999.

Gilmore, M. S. and Straka, J. M.: The Berry and Reinhardt Autoconversion Parameterization: A Digest, J. Appl. Meteor. Clim., 47, 375-396, https://doi.org/10.1175/2007JAMC1573.1, 2008.

Gilmore, M. S., Straka, J. M., and Rasmussen, E. N.: Precipitation uncertainty due to variations in precipitation particle parameters within a simple microphysics scheme, Mon. Wea. Rev., 132, 2610-2627, https://doi.org/10.1175/MWR2810.1, 2004.

Grabowski, W. W., Wu, X., and Moncrieff, M. W.: Cloud Resolving Modeling of Tropical Cloud Systems during Phase III of GATE. Part III: Effects of Cloud Microphysics, J. Atmos. Sci., 56, 2384-2402, https://doi.org/10.1175/1520-0469(1999)056<2384:CRMOTC>2.0.CO;2, 1999.

Grabowski, W. W.: Extracting Microphysical Impacts in Large-Eddy Simulations of Shallow Convection, J. Atmos. Sci., 71, 4493-4499, https://doi.org/10.1175/JAS-D-14-0231.1, 2014.

Grabowski, W. W., Morrison, H., Shima, S.-I., Abade, G. C., Dziekan, P., and Pawlowska, H.: Modeling of Cloud Microphysics: Can We Do Better?, Bull. Amer. Meteor. Soc., 100, 655-672, https://doi.org/10.1175/BAMS-D-18-0005.1, 2019.

Griffin, B. M. and Larson, V. E.: Analytic upscaling of a local microphysics scheme. Part II: Simulations, Quart. J. Royal Meteor. Soc., 139, 58-69, https://doi.org/10.1002/qj.1966, 2013.

Hong, S.-Y., Noh, Y., and Dudhia, J.: A new vertical diffusion package with an explicit treatment of entrainment processes, Mon. Wea. Rev., 134, 2318-2341, https://doi.org/10.1175/MWR3199.1, 2006.

Houghton, J. T., Ding, Y. H., Griggs, D. J., Noguer, M., Linden, P. J. v. d., Dai, X., K.Maskell, and Johnson, C. A. (Eds.): Climate Change 2001:The Scientific Basis, Cambridge University Press, Cambridge, 49 pp., 2001.

Hsieh, W. C., Jonsson, H., Wang, L. P., Buzorius, G., Flagan, R. C., Seinfeld, J. H., and Nenes, A.: On the representation of droplet coalescence and autoconversion: Evaluation using ambient cloud droplet size distributions, J. Geophys. Res.: Atmos., 114, https://doi.org/10.1029/2008JD010502, 2009.

Iacobellis, S. F. and Somerville, R. C. J.: Evaluating parameterizations of the autoconversion process using a single-column model and Atmospheric Radiation Measurement Program measurements, J. Geophys. Res.: Atmos., 111, n/a-n/a, https://doi.org/10.1029/2005jd006296, 2006.

Janjić, Z. I.: The step-mountain eta coordinate model: further developments of the convection, viscous sublayer, and turbulence closure schemes, Mon. Wea. Rev., 122, 927-945, https://doi.org/10.1175/1520-0493(1994)122<0927:TSMECM>2.0.CO;2, 1994.

Jing, X., Suzuki, K., and Michibata, T.: The Key Role of Warm Rain Parameterization in Determining the Aerosol Indirect Effect in a Global Climate Model, J. Climate, 32, 4409-4430, https://doi.org/10.1175/JCLI-D-18-0789.1, 2019.

Kain, J. S.: The Kain–Fritsch Convective Parameterization: An Update, J. Appl. Meteor., 43, 170-181, https://doi.org/10.1175/1520-0450(2004)043<0170:TKCPAU>2.0.CO;2, 2004.

Kessler, E.: On the Distribution and Continuity of Water Substance in Atmospheric Circulations, Circulations. Meteor. Monogr., 10. American Meteorological Society, Boston1969.

Khain, A. P., Beheng, K. D., Heymsfield, A., Korolev, A., Krichak, S. O., Levin, Z., Pinsky, M., Phillips, V., Prabhakaran, T., Teller, A., van den Heever, S. C., and Yano, J. I.: Representation of microphysical processes in cloud-resolving models: Spectral (bin) microphysics versus bulk parameterization, Rev. Geophys., 53, 2014RG000468, https://doi.org/10.1002/2014RG000468, 2015.

Khairoutdinov, M. and Kogan, Y.: A New Cloud Physics Parameterization in a Large-Eddy Simulation Model of Marine Stratocumulus, Mon. Wea. Rev., 128, 229-243, https://doi.org/10.1175/1520-0493(2000)128<0229:ancppi>2.0.co;2, 2000.

Kogan, Y. and Ovchinnikov, M.: Formulation of Autoconversion and Drop Spectra Shape in Shallow Cumulus Clouds, J. Atmos. Sci., 77, 711-722, https://doi.org/10.1175/JAS-D-19-0134.1, 2019.

Kong, F. and Yau, M. K.: An explicit approach to microphysics in MC2, Atmos.-Ocean, 35, 257-291, https://doi.org/10.1080/07055900.1997.9649594, 1997.

Krueger, S. K., Fu, Q., Liou, K. N., and Chin, H.-N. S.: Improvements of an Ice-Phase Microphysics Parameterization for Use in Numerical Simulations of Tropical Convection, J. Appl. Meteor., 34, 281-287, https://doi.org/10.1175/1520-0450-34.1.281, 1995.

Lee, H. and Baik, J.-J.: A physically based autoconversion parameterization, J. Atmos. Sci., 74, 1599-1616, https://doi.org/10.1175/JAS-D-16-0207.1, 2017.

Lei, H., Guo, J., Chen, D., and Yang, J.: Systematic Bias in the Prediction of Warm-Rain Hydrometeors in the WDM6 Microphysics Scheme and Modifications, J. Geophys. Res.: Atmos., 125, e2019JD030756, https://doi.org/10.1029/2019JD030756, 2020.

Lewis, J. M.: Roots of Ensemble Forecasting, Mon. Wea. Rev., 133, 1865-1885, https://doi.org/10.1175/MWR2949.1, 2005.

Li, M., Luo, Y., Zhang, D.-L., Chen, M., Wu, C., Yin, J., and Ma, R.: Analysis of a record-breaking rainfall event associated with a monsoon coastal megacity of south China using multi-source data, IEEE Trans. Geosci. Remote Sens., https://doi.org/ 10.1109/TGRS.2020.3029831, 2020.

Li, X.-Y., Brandenburg, A., Svensson, G., Haugen, N. E. L., Mehlig, B., and Rogachevskii, I.: Condensational and Collisional Growth of Cloud Droplets in a Turbulent Environment, J. Atmos. Sci., 77, 337-353, https://doi.org/10.1175/JAS-D-19-0107.1, 2019.

Lin, B., Zhang, J., and Lohmann, U.: A New Statistically based Autoconversion rate Parameterization for use in Large-Scale Models, J. Geophys. Res. : Atmos., 107, https://doi.org/10.1029/2001JD001484, 2002.

Liu, Y. and Daum, P. H.: Parameterization of the Autoconversion Process.Part I: Analytical Formulation of the Kessler-Type Parameterizations, J. Atmos. Sci., 61, 1539-1548, https://doi.org/10.1175/1520-0469(2004)061<1539:POTAPI>2.0.CO;2, 2004.

Liu, Y., Daum, P. H., McGraw, R., and Wood, R.: Parameterization of the Autoconversion Process. Part II: Generalization of Sundqvist-Type Parameterizations, J. Atmos. Sci., 63, 1103-1109, https://doi.org/10.1175/jas3675.1, 2006.

Manton, M. J. and Cotton, W. R.: Parameterization of the Atmospheric Surface Layer, J. Atmos. Sci., 34, 331-334, https://doi.org/10.1175/1520-0469(1977)034<0331:POTASL>2.0.CO;2, 1977a.

Manton, M. l. and Cotton, W. R.: Formulation of Approximate Equations for Modeling Moist Deep Convection on the Mesoscale. Atmospheric Science Paper 266, Colorado State University, 62 pp, 1977b.

McCumber, M., Tao, W.-K., Simpson, J., Penc, R., and Soong, S.-T.: Comparison of Ice-Phase Microphysical Parameterization Schemes Using Numerical Simulations of Tropical Convection, J. Appl. Meteor., 30, 985-1004, https://doi.org/10.1175/1520-0450-30.7.985, 1991.

Michibata, T. and Takemura, T.: Evaluation of autoconversion schemes in a single model framework with satellite observations, J. Geophys. Res.: Atmos., 120, 9570-9590, https://doi.org/10.1002/2015JD023818, 2015.

Mlawer, E. J., Taubman, S. J., Brown, P. D., Iacono, M. J., and Clough, S. A.: Radiative transfer for inhomogeneous atmospheres: RRTM, a validated correlated-k model for the longwave, J. Geophys. Res.: Atmos., 102, 16663-16682, https://doi.org/10.1029/97JD00237, 1997.

Morrison, H., Thompson, G., and Tatarskii, V.: Impact of Cloud Microphysics on the Development of Trailing Stratiform Precipitation in a Simulated Squall Line :

Comparison of One-and Two-Moment Schemes, Mon. Wea. Rev., 137, 991-1007, https://doi.org/10.1175/2008MWR2556.1, 2009.

Morrison, H., van Lier-Walqui, M., Fridlind, A. M., Grabowski, W. W., Harrington, J. Y., Hoose, C., Korolev, A., Kumjian, M. R., Milbrandt, J. A., Pawlowska, H., Posselt, D. J., Prat, O. P., Reimel, K. J., Shima, S.-I., van Diedenhoven, B., and Xue, L.: Confronting the Challenge of Modeling Cloud and Precipitation Microphysics, J. Adv. Model. Earth Sy., 12, e2019MS001689, https://doi.org/10.1029/2019MS001689, 2020.

Naeger, A. R., Colle, B. A., Zhou, N., and Molthan, A.: Evaluating Warm and Cold Rain Processes in Cloud Microphysical Schemes Using OLYMPEX Field Measurements, Mon. Wea. Rev., 148, 2163-2190, https://doi.org/10.1175/MWR-D-19-0092.1, 2020.

Niu, G.-Y., Yang, Z.-L., Mitchell, K. E., Chen, F., Ek, M. B., Barlage, M., Kumar, A., Manning, K., Niyogi, D., Rosero, E., Tewari, M., and Xia, Y.: The community Noah land surface model with multiparameterization options (Noah-MP): 1. Model description and evaluation with local-scale measurements, J. Geophys. Res.: Atmos., 116, D12109, https://doi.org/10.1029/2010JD015139, 2011.

Onishi, R., Matsuda, K., and Takahashi, K.: Lagrangian Tracking Simulation of Droplet Growth in Turbulence–Turbulence Enhancement of Autoconversion Rate*, J. Atmos. Sci., 72, 2591-2607, https://doi.org/10.1175/JAS-D-14-0292.1, 2015.

Pawlowska, H., and Brenguier, J. L.: A study of the microphysical structure of stratocumulus clouds. Proc. 12th Int. Conf. Clouds and precipitation, Zurich, Ed. P. R. Jones, Published by Page Bros., Norwich, U.K., 123-126, 1996.

Posselt, D. J., He, F., Bukowski, J., and Reid, J. S.: On the Relative Sensitivity of a Tropical Deep Convective Storm to Changes in Environment and Cloud Microphysical Parameters, J. Atmos. Sci., 76, 1163-1185, https://doi.org/10.1175/JAS-D-18-0181.1, 2019.

Randall, D. A., Bitz, C. M., Danabasoglu, G., Denning, A. S., Gent, P. R., Gettelman, A., Griffies, S. M., Lynch, P., Morrison, H., Pincus, R., and Thuburn, J.: 100 Years of Earth System Model Development, Meteor. Monogr., 59, 12.11-12.66, https://doi.org/10.1175/AMSMONOGRAPHS-D-18-0018.1, 2019.

Reen, B.: A brief guide to observation nudging in WRF, https://www2.mmm.ucar.edu/wrf/users/docs/ObsNudgingGuide.pdf, 2016.

Reisner, J., Rasmussen, R. M., and Bruintjes, R. T.: Explicit forecasting of supercooled liquid water in winter storms using the MM5 mesoscale model, Quart. J. Roy. Meteor. Soc., 124, 1071-1107, https://doi.org/10.1002/qj.49712454804 1998.

Rutledge, S. A. and Hobbs, P. V.: The Mesoscale and Microscale Structure and Organization of Clouds and Precipitation in Midlatitude Cyclones. XII: A Diagnostic Modeling Study of Precipitation Development in Narrow Cold-Frontal Rainbands, J. Atmos. Sci., 41, 2949-2972, https://doi.org/10.1175/1520-0469(1984)041<2949:TMAMSA>2.0.CO;2, 1984.

Schultz, P.: An Explicit Cloud Physics Parameterization for Operational Numerical Weather Prediction, Mon. Wea. Rev., 123, 3331-3343, https://doi.org/10.1175/1520-0493(1995)123<3331:AECPPF>2.0.CO;2, 1995.

Seifert, A. and Beheng, K. D.: A double-moment parameterization for simulating autoconversion, accretion and selfcollection, Atmos. Res., 59-60, 265-281, https://doi.org/10.1016/S0169-8095(01)00126-0, 2001.

Seifert, A., Nuijens, L., and Stevens, B.: Turbulence effects on warm-rain autoconversion in precipitating shallow convection, Quart. J. Royal Meteor. Soc., 136, 1753-1762, https://doi.org/10.1002/qj.684, 2010.

Silverman, B. A. and Glass, M.: A Numerical Simulation of Warm Cumulus Clouds: Part I. Parameterized vs Non-Parameterized Microphysics, J. Atmos. Sci., 30, 1620-1637, https://doi.org/10.1175/1520-0469(1973)030<1620:ANSOWC>2.0.CO;2, 1973.

Simpson, j. and Wiggert, v.: Models of precipitating cumulus towers, Mon. Wea. Rev., 97, 471-489, https://doi.org/10.1175/1520-0493(1969)097<0471:MOPCT>2.3.CO;2, 1969.

Skamarock, W. C., Klemp, J. B., Duda, M. G., Fowler, L. D., Park, S.-H., and Ringler, T. D.: A Multiscale Nonhydrostatic Atmospheric Model Using Centroidal Voronoi Tesselations and C-Grid Staggering, Mon. Wea. Rev., 140, 3090-3105, https://doi.org/10.1175/MWR-D-11-00215.1, 2012.

Skamarock, W. C., Klemp, J. B., Dudhia, J., Gill, D. O., Liu, Z., Berner, J., Wang, W., Powers, J. G., Duda, M. G., Barker, D. M., and Huang, X.-Y.: A Description of the Advanced Research WRF Version 4. NCAR Tech. Note NCAR/TN-556+STR, 145 pp, https://doi.org/10.5065/1dfh-6p97, 2019.

Sundqvist, H., Berge, E., and Kristjánsson, J. E.: Condensation and Cloud Parameterization Studies with a Mesoscale Numerical Weather Prediction Model, Mon. Wea. Rev., 117, 1641-1657, https://doi.org/10.1175/1520-0493(1989)117<1641:cacpsw>2.0.co;2, 1989.

Tao, W.-K. and Simpson, J.: Goddard Cumulus Ensemble Model. Part I: Model Description, Terr. Atmos. Oceanic Sci., 4, 35-72, https://doi.org/10.3319/TAO.1993.4.1.35(A), 1993.

Tapiador, F. J., Sánchez, J.-L., and García-Ortega, E.: Empirical values and assumptions in the microphysics of numerical models, Atmos. Res., 215, 214-238, https://doi.org/10.1016/j.atmosres.2018.09.010, 2019.

Thompson, G., Rasmussen, R. M., and Manning, K.: Explicit Forecasts of Winter Precipitation Using an Improved Bulk Microphysics Scheme. Part I: Description and Sensitivity Analysis, Mon. Wea. Rev., 132, 519-542, https://doi.org/10.1175/1520-0493(2004)132<0519:EFOWPU>2.0.CO;2, 2004.

Thompson, G., Field, P. R., Rasmussen, R. M., and Hall, W. D.: Explicit Forecasts of Winter Precipitation Using an Improved Bulk Microphysics Scheme. Part II: Implementation of a New Snow Parameterization, Mon. Wea. Rev., 136, 5095-5115, https://doi.org/10.1175/2008MWR2387.1, 2008.

Wellmann, C., Barrett, A. I., Johnson, J. S., Kunz, M., Vogel, B., Carslaw, K. S., and Hoose, C.: Comparing the impact of environmental conditions and microphysics on the forecast uncertainty of deep convective clouds and hail, Atmos. Chem. Phys., 20, 2201-2219, https://doi.org/10.5194/acp-20-2201-2020, 2020.

White, B., Gryspeerdt, E., Stier, P., Morrison, H., Thompson, G., and Kipling, Z.: Uncertainty from the choice of microphysics scheme in convection-permitting models significantly exceeds aerosol effects, Atmos. Chem. Phys., 17, 12145-12175, https://doi.org/10.5194/acp-17-12145-2017, 2017.

Wood, R.: Drizzle in Stratiform Boundary Layer Clouds. Part II: Microphysical Aspects, J. Atmos. Sci., 62, 3034-3050, https://doi.org/10.1175/JAS3530.1, 2005.

Wood, R. and Blossey, P. N.: Comments on “Parameterization of the Autoconversion Process. Part I: Analytical Formulation of the Kessler-Type Parameterizations”, J. Atmos. Sci., 62, 3003-3006, https://doi.org/10.1175/jas3524.1, 2005.

Wood, R., Field, P. R., and Cotton, W. R.: Autoconversion rate bias in stratiform boundary layer cloud parameterizations, Atmos. Res., 65, 109-128, http://dx.doi.org/10.1016/S0169-8095(02)00071-6, 2002.

Xiao, H., Yin, Y., Zhao, P., Wan, Q., and Liu, X.: Effect of Aerosol Particles on Orographic Clouds: Sensitivity to Autoconversion Schemes, Advances in Atmospheric Sciences, 37, 229-238, https://doi.org/10.1007/s00376-019-9037-6, 2020.

Yin, J.-F., Wang, D.-H., Liang, Z.-M., Liu, C.-J., Zhai, G.-Q., and Wang, H.: Numerical Study of the Role of Microphysical Latent Heating and Surface Heat Fluxes in a Severe Precipitation Event in the Warm Sector over Southern China, Asia-Pacific J. Atmos. Sci., 54, 77-90, https://doi.org/10.1007/s13143-017-0061-0, 2018.

Yin, J., Wang, D., and Zhai, G.: An attempt to improve Kessler-type parameterization of warm cloud microphysical conversion processes using CloudSat observations, J. Meteorol. Res., 29, 82-92, https://doi.org/10.1007/s13351-015-4091-1, 2015.

Yin, J., Zhang, D.-L., Luo, Y., and Ma, R.: On the Extreme Rainfall Event of 7 May 2017 Over the Coastal City of Guangzhou. Part I: Impacts of Urbanization and Orography, Mon. Wea. Rev., https://doi.org/10.1175/MWR-D-19-0212.1, 2020.

Yuter, S. E. and Houze, R. A.: Three-Dimensional Kinematic and Microphysical Evolution of Florida Cumulonimbus. Part II: Frequency Distributions of Vertical Velocity, Reflectivity, and Differential Reflectivity, Mon. Wea. Rev., 123, 1941-1963, https://doi.org/10.1175/1520-0493(1995)123<1941:TDKAME>2.0.CO;2, 1995.

Zhang, Y., Li, J., Yu, R., Zhang, S., Liu, Z., Huang, J., and Zhou, Y.: A Layer-Averaged Nonhydrostatic Dynamical Framework on an Unstructured Mesh for Global and Regional Atmospheric Modeling: Model Description, Baseline Evaluation, and Sensitivity Exploration, J. Adv. Model. Earth Sy., 11, 1685-1714, https://doi.org/10.1029/2018MS001539, 2019

Figures

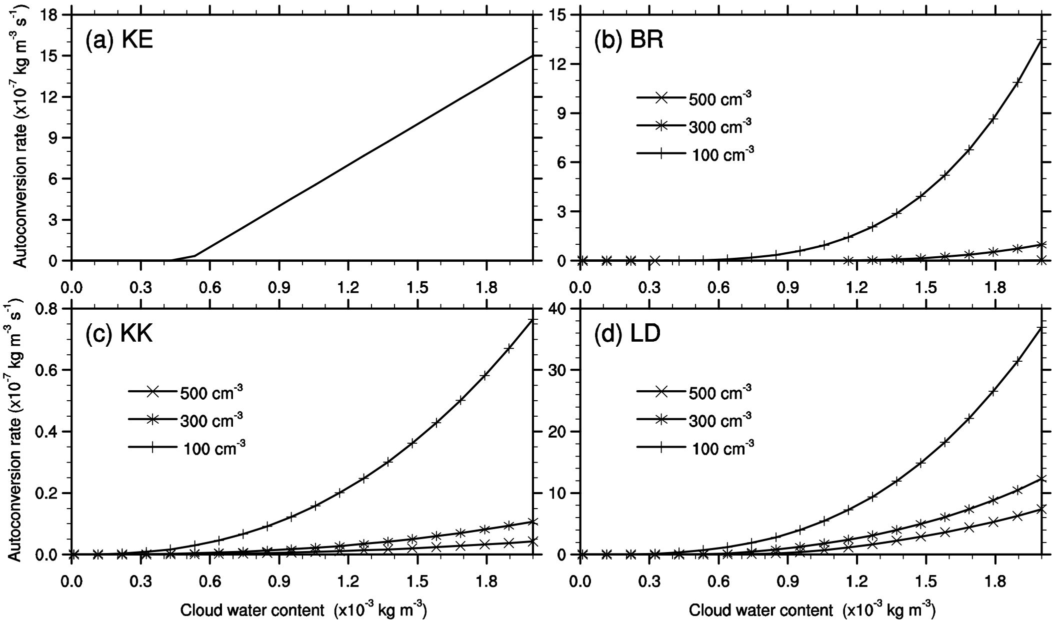

Fig. 1 Evolution of autoconversion rates with a wide range of cloud water content at given cloud number concentrations (N_c) of 100 cm^{-3}, 300 cm^{-3}, and 500 cm^{-3}, respectively. (a) KE denotes the Kessler scheme (1969), and (b) BR indicates the Berry and Reinhardt scheme (1974); (c) KK and (d) LD represents the Khairoutdinov and Kogan (2000) and Liu et al. (LD) schemes (2006), respectively.

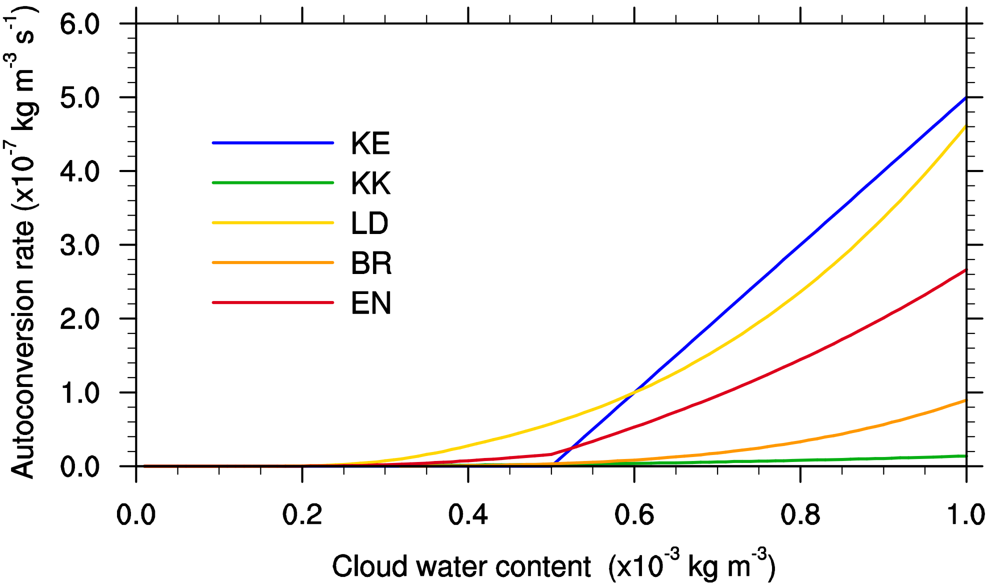

Fig. 2 Comparisons of the EN scheme with the selected KE, BR, KK, and LD schemes at a fixed N_c of 300 cm^{-3}. (see text for further details)

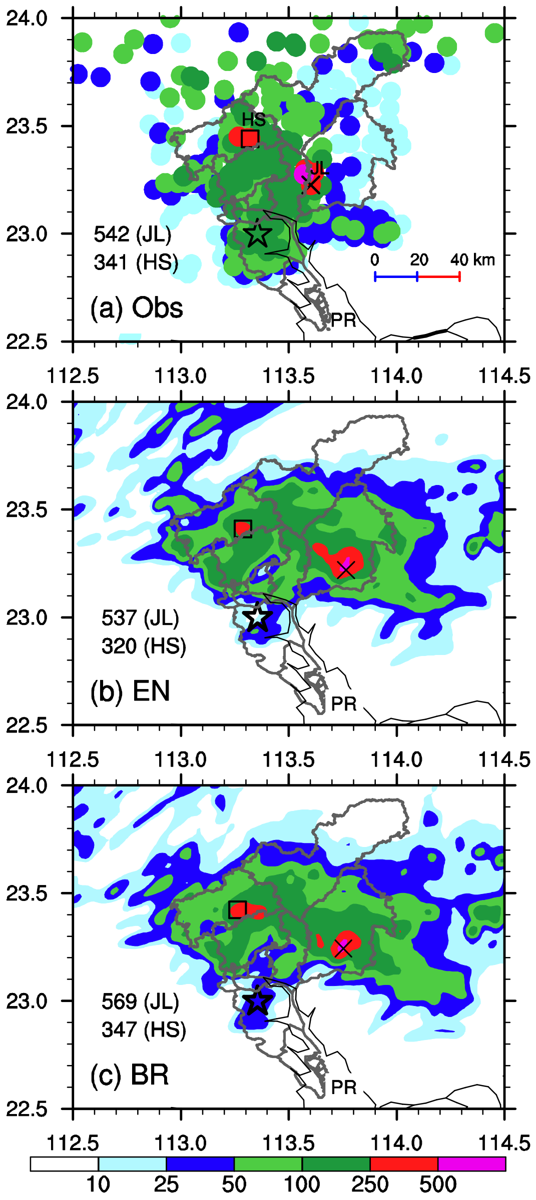

Fig. 3 Spatial distribution of the 18-h accumulated rainfall during the period of 2000 BST 6 May to 1400 BST 7 May, 2017: (a) rain gauge observations and (b-c) simulations with the EN and BR autoconversion schemes. A cross sign (×) and a square sign (□) denote the locations where maximum hourly rainfall rates were (a) observed or (b-c) simulated near Jiulong (JL) and Huashan(HS), respectively. The values marked with JL and HS indicate the 18-h maximum accumulated rainfall amounts near the JL and HS, respectively. A star indicates the city center of Guangzhou, and the Pearl River is marked by PR; similarly for the rest of figures.

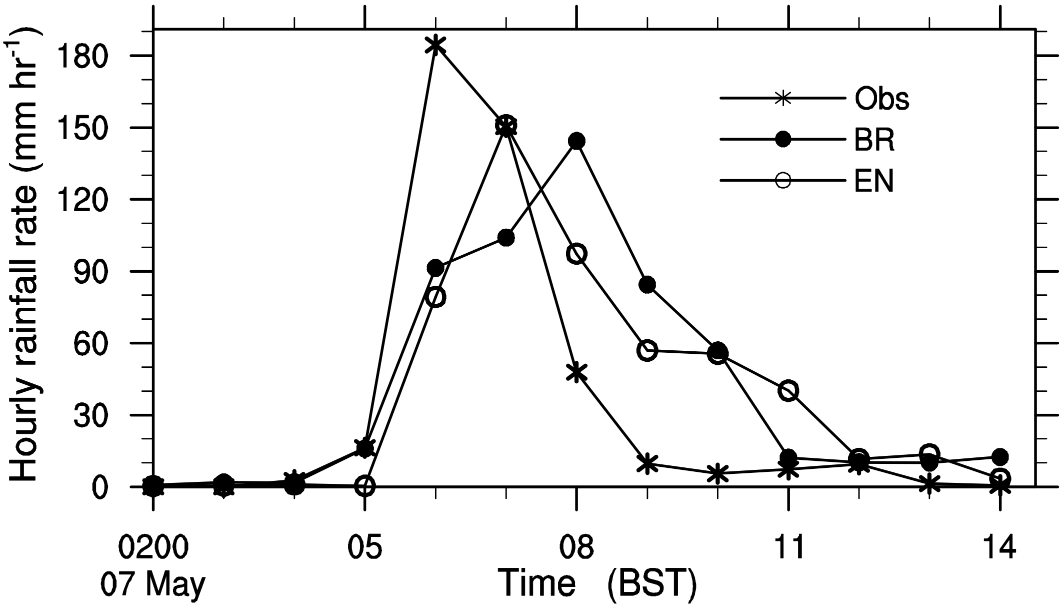

Fig. 4 Time series of hourly rainfall rates (mm hr^{-1}) from rain gauge observations (asterisks) and simulated with the EN scheme (circles) and the BR scheme (dots) near Jiulong during the period of 2000 BST 6 - 1400 BST 7 May 2017. (see Fig. 3 for their locations)

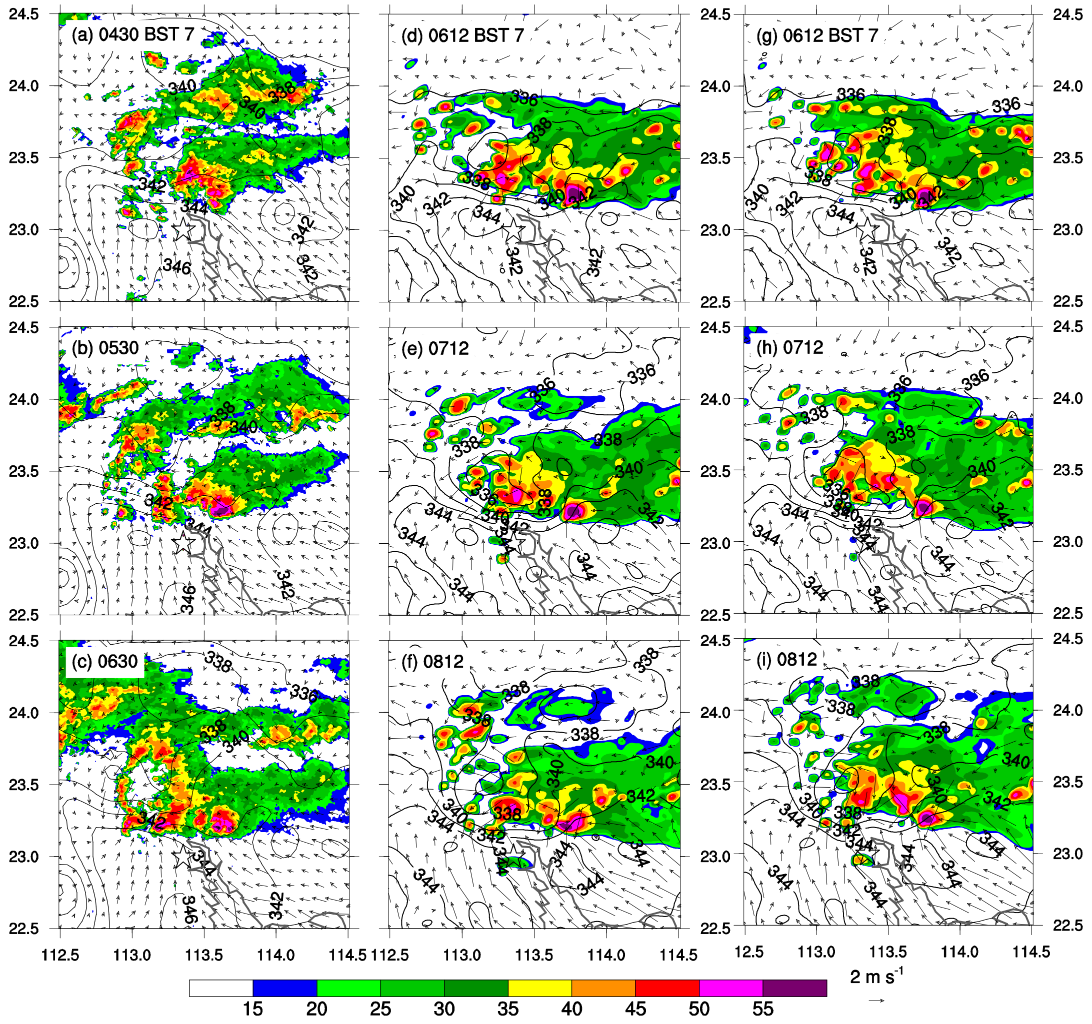

Fig. 5 Horizontal maps of composite radar reflectivity (dBZ, shadings) and surface (z = 10 m) horizontal wind vectors and equivalent potential temperature (q_e, contoured at 2K intervals) during the extreme rainfall stage: (a-c) observed, (d-f) simulated with the EN scheme, and (g-i) simulated with the BR scheme. A reference wind vector is given beneath the right column next to the composite radar reflectivity color scale.

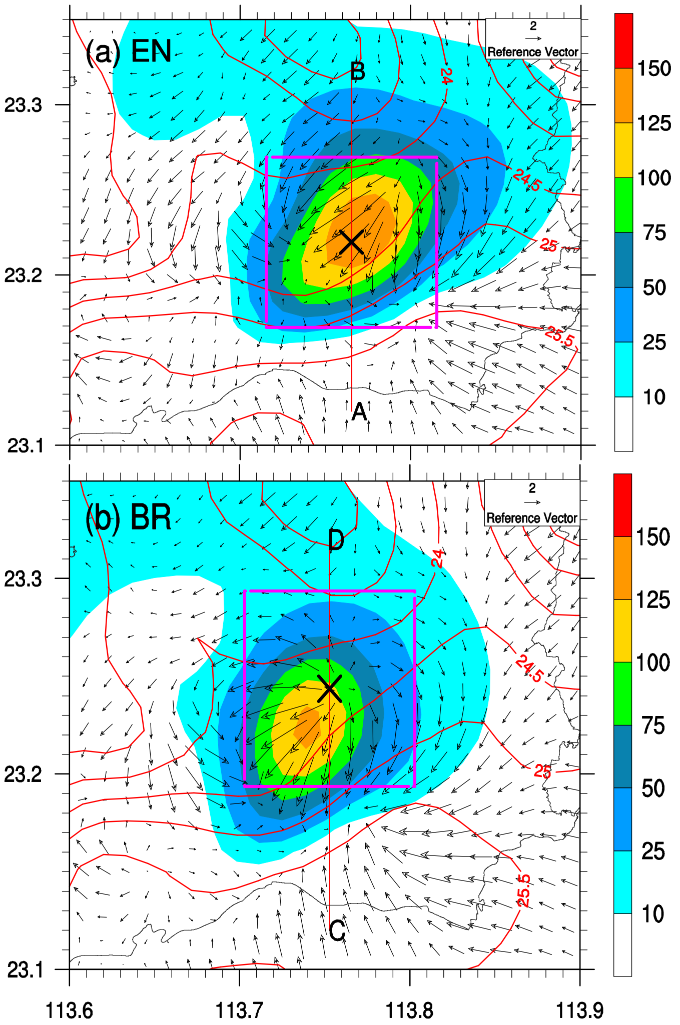

Fig. 6 Spatial distribution of hourly rainfall amount (mm, shadings), temporal-averaged surface temperature (contoured at 0.5℃ intervals) and horizontal wind fields (vectors) during the period from 0600 BST to 0700 BST 7 May, 2017. The red lines, A-B and C-D, indicate the locations of the vertical cross section in Fig. 7. The two pink-squared boxes, covering an area of 0.1° × 0.1° with the center of the maximum hourly rainfall, are marked for domain-averaged in Fig. 8 and Fig. 9.

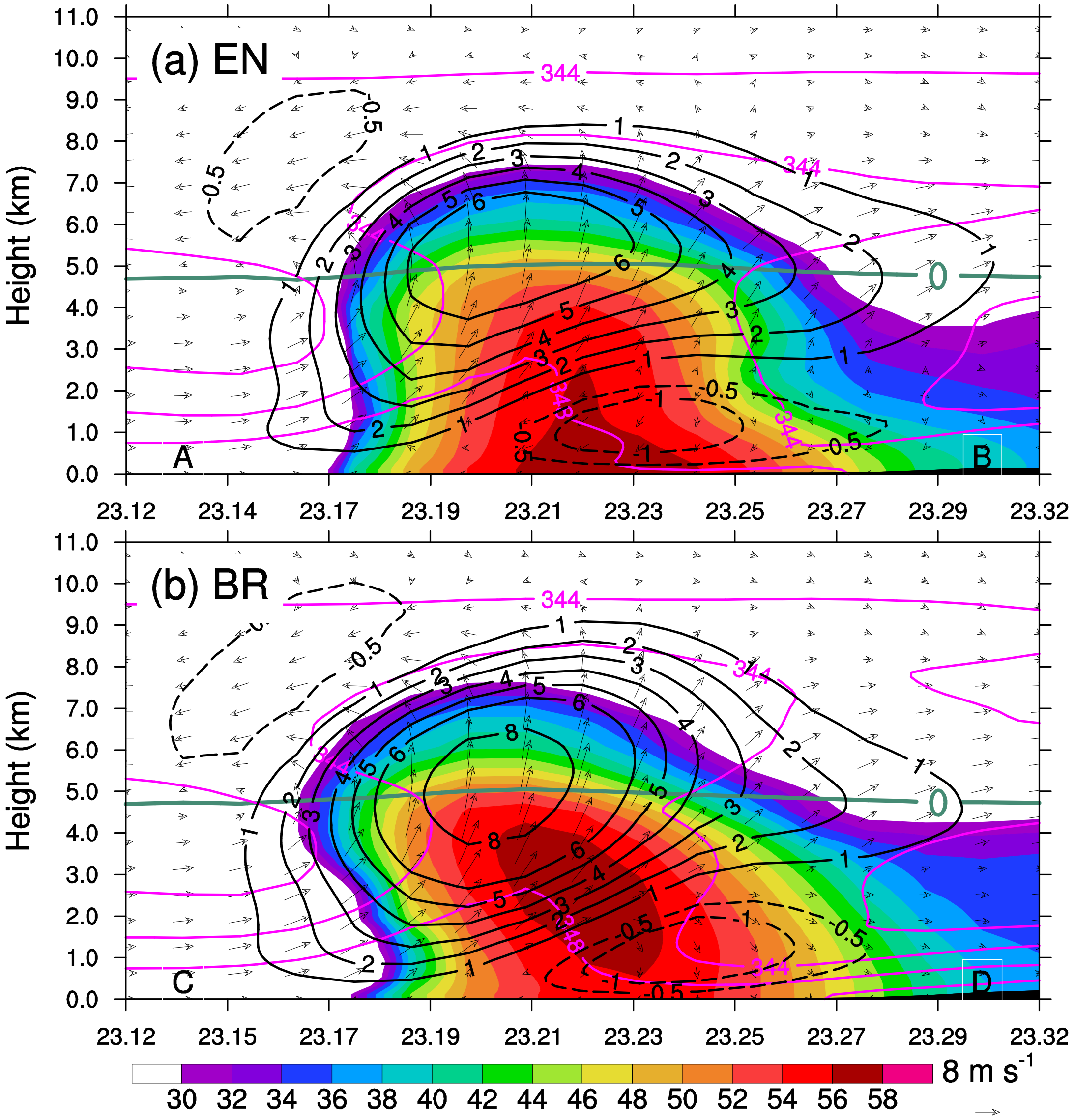

Fig. 7 Temporal-averaged vertical cross sections along (a) A-B and (b) C-D in Fig. 6 of the simulated reflectivity (dBZ, shadings), vertical velocity (black contours, m s^{-1}), in-plane flow vectors (vertical motion amplified by a factor of 2), and theta-e(θ_e, pink-contoured at 4K intervals) during the period from 0600 BST to 0700 BST 7 May, 2017. Thick light green line indicates an isotherm of 0°C.

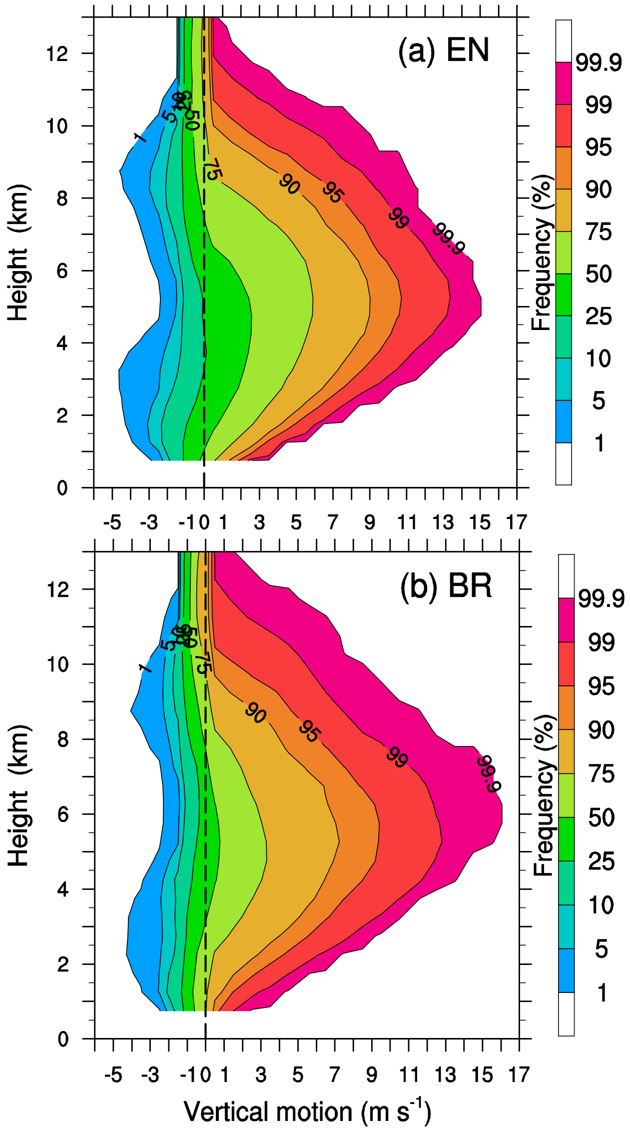

Fig. 8 CCFADs of the simulated vertical motion for (a) the EN scheme and (b) the BR scheme within the respective boxes marked with pink lines in Fig. 6. The CCFADs are calculated from eleven model outputs with six-minute intervals during the severe rainfall episode from 0600 BST to 0700 BST 7 May, 2017.

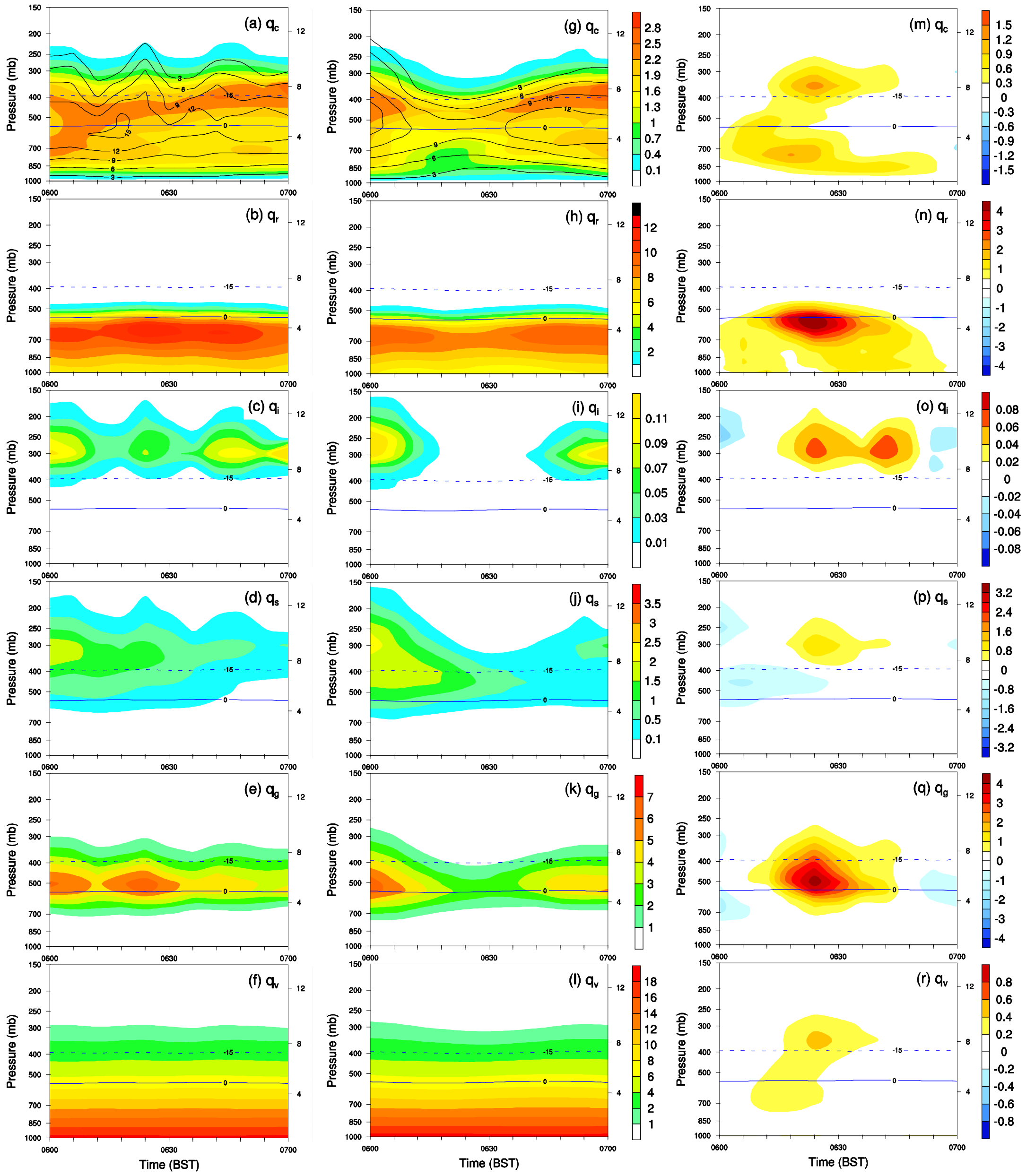

Fig. 9 Comparison of time-height cross sections of domain-averaged mixing ratios between the EN scheme (a-f) and the BR scheme (g-i) during the period from 0600 BST to 0700 BST 7 May, 2017, within the domains marked with pink lines in Fig. 6. q_c, q_r, q_i, q_s, and q_g denotes cloud water, rainwater, cloud ice, snow, and graupel, respectively. (m-r) gives the differences between EN and BR (i.e, EN – BR). Thick blue lines indicate isotherm of -15°C and 0°C, respectively.